THE ASTROPHYSICAL JOURNAL, 463:191–204, 1996 May 20


# ULTRAVIOLET-EXCITED $H_2$: A COMPARISON WITH LARGE-SCALE TRACERS OF MOLECULAR CLOUDS

M. L. LUHMAN[1] AND D. T. JAFFE
Department of Astronomy, University of Texas at Austin, Austin, TX 78712
*Received 1995 August 3; accepted 1995 November 27*

## ABSTRACT

We present observations of the 1.601 $\mu$m $v = 6$–4 $Q(1)$, 2.121 $\mu$m $v = 1$–0 $S(1)$, and 2.247 $\mu$m $v = 2$–1 $S(1)$ lines of $H_2$ from four galactic clouds: the Orion A and Orion B giant molecular clouds, the $\rho$ Ophiuchi cloud, and the G236+39 interstellar cirrus cloud. We employed the University of Texas Near-Infrared Fabry-Perot Spectrometer to conduct the first survey of diffuse ($\lesssim 10^{-5}$ ergs s$^{-1}$ cm$^{-2}$ sr$^{-1}$) $H_2$ emission from galactic clouds on multiparsec scales. The relative strengths of the $H_2$ lines suggest that, on large scales, excitation of $H_2$ via ultraviolet fluorescence is a common phenomenon. We compare the distribution and strength of the $H_2$ emission to cospatial observations of the 158 $\mu$m line of $C^+$, the low rotational level lines of $^{13}CO$ and $^{12}CO$, and the 60 and 100 $\mu$m continuum radiation. This comparative study shows that (1) ultraviolet-excited $H_2$ and $C^+$ correlate spatially, consistent with theoretical models of photon-dominated environments; (2) $H_2$ emission arises from significant portions of CO clouds but can also extend into regions where much of the CO is dissociated; and (3) there is a significant correlation between the $H_2$ line intensity and the far-infrared continuum, which we attribute to ultraviolet illumination of $H_2$ and dust on cloud surfaces. We discuss the implications of this study for using CO and the far-infrared continuum to trace molecular gas, as well as for the future role of $H_2$ as a complement to other large-scale probes of the dense interstellar medium.

*Subject headings:* infrared: ISM: lines and bands — ISM: clouds — ISM: individual (Orion, NGC 2024, $\rho$ Ophiuchi) — ISM: molecules — molecular processes

## 1. INTRODUCTION

This paper presents observations of the $H_2$ emission from the surfaces of galactic molecular clouds and compares the $H_2$ emission to other probes of the large-scale morphology and physical properties of the molecular clouds. Molecular hydrogen, the most abundant interstellar molecule, has a small moment of inertia, which means that its low-lying rotational energy levels are well separated. Conventional wisdom says that emission from $H_2$ is not seen outside energetic star-forming regions or environments with strong ultraviolet fields because, unlike heavier molecules such as CO, no excited levels are thermally populated in cold ($T \lesssim 100$ K) clouds. We have recently shown, however, that we can detect vibrationally excited $H_2$ emission in the near-IR from the UV-exposed surfaces of molecular clouds over large scales (Luhman et al. 1994) using an instrument optimized for surface brightness sensitivity (Luhman et al. 1995). How can $H_2$ complement other tracers of molecular material? What are the potential uses of large-scale $H_2$ emission? We analyze here new $H_2$ observations in order to address these questions.

Molecular hydrogen line emission in the near-IR arises where UV photons strike molecular cloud surfaces. In the cloud surface layer, commonly known as the photodissociation or photon-dominated region (PDR), UV photons ionize atoms, dissociate molecules, and contribute significantly to gas heating by ejecting electrons from dust grains and by directly exciting atoms and molecules (see, e.g., de Jong, Dalgarno, & Boland 1980; Tielens & Hollenbach 1985a; Black & van Dishoeck 1987; van Dishoeck & Black 1988; Sternberg & Dalgarno 1989; Burton, Hollenbach, & Tielens 1990; Dalgarno 1992; Roger & Dewdney 1992; Sternberg 1992; Le Bourlot et al. 1993). In a PDR, the observed $H_2$ electric quadrupole ro-vibrational transitions in the near-IR usually arise as a result of a radiative fluorescent cascade following UV excitation (Black & van Dishoeck 1987). In some cases, collisions in gas heated by the UV radiation can excite the lowest vibrational levels (Sternberg & Dalgarno 1989; Luhman et al. 1996). In regions with significant supersonic gas motions, shock heating can also contribute to the excitation of the lower lying ro-vibrational levels. The emergent spectra of UV-excited and collisionally excited $H_2$ have distinct characteristics. Observations of well-chosen low ($v \leq 2$) and high ($v > 2$) vibrational transitions can determine unambiguously which excitation mechanism is at work.

Selection biases led the first observers of the 2 $\mu$m line emission of $H_2$ to find line intensity ratios consistent with collisional excitation in shock-heated gas (e.g., Shull & Beckwith 1982; Beckwith et al. 1983). Over the past two decades, however, several groups have predicted that $H_2$ should also arise in PDRs and have modeled the emergent spectrum (e.g., Black & Dalgarno 1976; Shull 1978; Black & van Dishoeck 1987; Sternberg 1988; Sternberg & Dalgarno 1989). Observations of $H_2$ lines, as well as [C II], [O I], and CO lines, have demonstrated that PDR models can explain the emission from some local (0.1–0.5 pc) regions close to luminous OB stars (i.e., with UV fields of $10^3$–$10^6$ times the mean field in the solar neighborhood; Tielens & Hollenbach 1985b; Black & van Dishoeck 1987; Burton et al. 1990). These regions include the Orion bright bar (Hayashi et al. 1985), the reflection nebulae Parsamyan 18 (Sellgren 1986) and NGC 2023 (Hasegawa et al. 1987; Gatley & Kaifu 1987; Gatley et al. 1987), the planetary

[1] Current address: Naval Research Laboratory, Remote Sensing Division, Code 7217, Washington, DC 20375-5351.

TABLE 1

OBSERVING PARAMETERS

| SOURCE | (0, 0) POSITION[a] $\alpha_{1950}$ | (0, 0) POSITION[a] $\delta_{1950}$ | SKY OFFSET[b] | BEAM SIZE |
|---|---|---|---|---|
| Orion A | $5^h32^m49^s.0$ | −05°25′16″ | ... | ... |
| E20′–W10′ | ... | ... | W2° | 49″ |
| E20′–E76′, W10′–W34′ | ... | ... | W2° | 65 |
| "Ridge" | ... | ... | W2° | 49 |
| Orion B/NGC 2024 | 5 39 49.0 | −01 57 00 | ... | ... |
| E3′–W15′ | ... | ... | W2° | 65 |
| W15′–W19′ | ... | ... | W17′ | 89 |
| Orion B/NGC 2023 | 5 39 07.3 | −02 16 58 | W2° | 65 |
| ρ Oph | 16 22 22.8 | −24 21 07 | N2° | 198 |
| G236+39 | 9 36 35.0 | 00 03 00 | W17′ | 89 |

[a] Orion A (0, 0) position: $\theta^1$ Ori C; NGC 2023: HD 37903; ρ Oph: HD 147889.
[b] Offset from the (0, 0) position.

nebula Hubble 12 (Dinerstein et al. 1988), and the H II region M17 (Gatley & Kaifu 1987; Tanaka et al. 1989). Until recently, however, there were no near-IR observations of UV-excited $H_2$ emission from galactic PDRs on large (1–10 pc) scales because of the intrinsically faint level and large angular extent of the $H_2$ emission.

Observations and models together imply that UV-excited (fluorescent) $H_2$ should exist, at some level, not only near OB stars but also over the entire surfaces of molecular clouds. We have now observed near-IR $H_2$ emission from the Orion A giant molecular cloud (Luhman et al. 1994) and the Galactic center (Pak, Jaffe, & Keller 1996) on degree scales. (Observations of electronic transitions in the UV have demonstrated the existence of UV-excited $H_2$ from the diffuse interstellar medium; Martin, Hurwitz, & Bowyer 1990.) As the number of observations of extended near-IR $H_2$ emission begins to grow, it is appropriate to explore the relationship of UV-excited $H_2$ emission to other large-scale tracers of molecular clouds. In this paper, we compare the emission in the near-IR $H_2$ lines, the [C II] $^2P_{3/2}$–$^2P_{1/2}$ 158 μm line, the low-$J$ lines of CO, and the 60 and 100 μm continuum radiation from dust grains. The low rotational lines of CO and the far-IR continuum radiation are commonly used as large-scale tracers, nominally of the cold, interior material that constitutes the bulk of the mass in molecular clouds. However, the UV-illuminated surfaces of molecular clouds can also give rise to CO and far-IR emission, as well as to $H_2$ lines (see, e.g., Tielens & Hollenbach 1985a; Maloney & Black 1988). Large-scale observations of the [C II] 158 μm line are a proven technique for highlighting PDR surfaces on multiparsec scales and are a logical choice for direct comparison with $H_2$ emission (see, e.g., Stutzki et al. 1988; Matsuhara et al. 1989; Howe et al. 1991; Stacey et al. 1993).

We have chosen four objects in which to study extended near-IR $H_2$ emission: the Orion A and Orion B giant molecular clouds, the ρ Ophiuchi cloud, and the G236+39 interstellar cirrus cloud. These sources are well mapped in [C II] 158 μm, CO, and/or the far-IR continuum and, except for G236+39, are exposed to UV radiation from O and B stars (i.e., UV fields of 10–$10^4$ times the solar neighborhood field). Our large-scale observations of Orion lie along cuts through the bright H II region M42 in Orion A and the H II region NGC 2024 and include observations of the reflection nebula NGC 2023. In Orion A, the OB stars of the Trapezium ($\theta^1$ Ori) cluster provide a copious supply of UV photons. The main exciting OB star(s) in NGC 2024 remain undetected as a result of a thick north-south dust lane that straddles the H II region. Near the western edge of the Orion B/NGC 2024 cloud, a bright external O star (ζ Ori) irradiates the cloud surface. In NGC 2023, the illuminating B star HD 37903 is the main source of UV radiation, and in ρ Oph four B stars (HD 147889, S1, SR 3, and σ Sco) associated with the cloud expose the surrounding molecular material to UV flux. The G236+39 cirrus cloud typifies a very low excitation environment, far from any identifiable source of UV radiation (Reach, Koo, & Heiles 1994). All four clouds are nearby (Orion A: 450 pc; Genzel & Stutzki 1989; NGC 2024: 415 pc; Anthony-Twarog 1982; NGC 2023: 475 pc; Lee 1968, de Boer 1983; ρ Oph: 160 pc; Whittet 1974; G236+39: ~100 pc; Reach et al. 1994), extend over at least several degrees, and lie out of the Galactic plane. Thus, a large number of environments per cloud with a wide range of excitation and physical conditions are observable with little line-of-sight confusion.

## 2. OBSERVATIONS

We observed the 2.121 μm $v = 1$–0 $S(1)$ transition of $H_2$ toward portions of the Orion A and B giant molecular clouds, the ρ Oph dark cloud, and the G236+39 interstellar cirrus cloud. For selected regions, we also observed the 1.601 μm $v = 6$–4 $Q(1)$ and 2.247 μm $v = 2$–1 $S(1)$ $H_2$ transitions. We used the University of Texas Near-Infrared Fabry-Perot Spectrometer with the McDonald Observatory 2.7 m telescope in 1992 October/December and 1994 January/February, the McDonald Observatory 0.9 m in 1994 June, the Steward Observatory 1.55 m telescope in 1994 February, and the Cerro Tololo Inter-American Observatory (CTIO) 1.5 m telescope in 1994 December. Luhman et al. (1995) detail the observing procedure and spectrometer design. The instrumental beam size (equivalent disk) is 49″ ($\Omega = 4.4 \times 10^{-8}$ sr) at the McDonald 2.7 m, 198″ ($\Omega = 7.24 \times 10^{-7}$ sr) at the McDonald 0.9 m, 65″ ($\Omega = 7.9 \times 10^{-8}$ sr) at the Steward 1.55 m, and 89″ ($\Omega = 1.46 \times 10^{-7}$ sr) at the CTIO 1.5 m.

We obtained the $H_2$ spectra by scanning a Fabry-Perot interferometer across the line profile. To remove the background signal, we obtained sky spectra, which were subtracted from spectra of the object. When observing the inner part of very extended clouds such as Orion and ρ Oph, we obtained sky spectra by nodding the telescope a few degrees

TABLE 2

OBSERVATIONS

| Position[b] | Line Intensity[a] ($10^{-5}$ ergs s$^{-1}$ cm$^{-2}$ sr$^{-1}$) $H_2$ $v=$ 1–0 $S(1)$ | $H_2$ $v=$ 2–1 $S(1)$ | $H_2$ $v=$ 6–4 $Q(1)$ |
|---|---|---|---|
| **Orion A East-West** | | | |
| (0, 0) | 30.3(1.1)[c,d] | 4.97(0.10)[d] | 0.73(0.12)[c,d] |
| (E2′, 0) | 5.1(1.3)[c,d] | 1.07(0.05)[d] | 0.49(0.10)[c,d] |
| (E4′, 0) | 3.3(1.0)[c,d] | 1.52(0.09)[d] | 0.44(0.09)[c,d] |
| (E6′, 0) | 2.8(0.6)[c] | 0.86(0.15) | ... |
| (E8′, 0) | 2.3(0.6)[c] | 0.84(0.07) | 0.39(0.05)[c] |
| (E10′, 0) | 2.8(0.5)[c] | ... | ... |
| (E12′, 0) | 0.52(0.16)[c] | 0.28(0.06) | 0.33(0.07)[c] |
| (E14′, 0) | 0.8(0.3)[c] | ... | ... |
| (E16′, 0) | 0.7(0.3)[c] | 0.22(0.06) | 0.25(0.09)[c] |
| (E20′, 0) | ... | 0.10(0.03) | 0.18(0.04)[c] |
| (E28′, 0) | 0.33(0.10)[c] | ... | ... |
| (E36′, 0) | 0.30(0.09)[c] | ... | ... |
| (E44′, 0) | 0.15(0.05)[c] | ... | ... |
| (E60′, 0) | 0.15(0.07)[c] | ... | ... |
| (W2′, 0) | 3.8(0.7)[c,d] | 0.78(0.04)[d] | 0.36(0.10)[c,d] |
| (W4′, 0) | 1.3(0.4)[c] | 0.58(0.15) | 0.21(0.06)[c] |
| (W6′, 0) | 0.6(0.3)[c] | 0.45(0.09) | 0.26(0.06)[c] |
| (W8′, 0) | 0.6(0.3)[c] | 0.34(0.05) | 0.27(0.09)[c] |
| (W18′, 0) | 1.3(0.2)[c] | ... | ... |
| (W26′, 0) | 0.15(0.05)[c] | ... | ... |
| **Orion A "Ridge"** | | | |
| (E11″, N59″) | 36.0(1.0) | ... | ... |
| (E22″, N118″) | 8.4(1.0)[d] | 2.53(0.15)[d] | 0.28(0.08)[d] |
| (E33″, N177″) | 4.4(0.5) | ... | ... |
| (E44″, N236″) | 5.2(0.7)[d] | 1.54(0.07)[d] | 0.25(0.03)[d] |
| (E66″, N354″) | 2.0(0.4)[d] | 0.90(0.08)[d] | 0.25(0.03)[d] |
| (E77″, N413″) | 1.4(0.5) | ... | ... |
| (E88″, N472″) | 1.5(0.5)[d] | 1.46(0.16)[d] | 0.34(0.06)[d] |
| (E99″, N531″) | 0.8(0.3) | ... | ... |
| (E110″, N590″) | 2.7(0.4)[d] | 1.23(0.06)[d] | 0.41(0.07)[d] |
| (E132″, N708″) | 3.9(0.6)[d] | 1.28(0.04)[d] | 0.24(0.04)[d] |
| (E154″, N826″) | 5.0(0.7)[d] | 1.05(0.08)[d] | 0.21(0.05)[d] |
| (E165″, N885″) | 3.9(0.6) | ... | ... |
| (E176″, N944″) | 0.49(0.09) | 0.20(0.03) | ... |
| (E187″, N1003″) | 1.3(0.5) | ... | ... |
| (E198″, N1062″) | ... | 0.16(0.05) | ... |
| (W22″, S118″) | 4.7(0.7)[d] | 2.11(0.11)[d] | 0.39(0.10)[d] |
| (W44″, S236″) | 2.20(0.07) | 1.07(0.06) | 0.38(0.06) |
| (W66″, S354″) | 2.2(0.8) | 0.73(0.06) | 0.36(0.16) |
| (W88″, S472″) | 1.10(0.16) | 0.44(0.07) | ... |
| (W110″, S590″) | 1.1(0.3) | 0.71(0.07) | ... |
| **Orion B/NGC 2024** | | | |
| (0, 0) | 1.9(0.3)[d] | 0.63(0.05)[d] | 0.19(0.12)[d] |
| (E1′, 0) | 2.0(0.4)[d] | 0.66(0.04)[d] | 0.44(0.10)[d] |
| (E2′, 0) | 1.7(0.2)[d] | 0.59(0.03)[d] | 0.53(0.10)[d] |
| (E3′, 0) | 0.74(0.11) | 0.27(0.05) | ... |
| (W1′, 0) | 2.25(0.18)[d] | 0.70(0.06)[d] | 0.25(0.15)[d] |
| (W2′, 0) | 1.91(0.13)[d] | 0.66(0.08)[d] | 0.36(0.11)[d] |
| (W3′, 0) | 1.34(0.07)[d] | 0.51(0.04)[d] | 0.43(0.12)[d] |
| (W4′, 0) | 1.3(0.3) | ... | ... |
| (W5′, 0) | 1.1(0.4) | ... | ... |
| (W6′, 0) | 0.8(0.3) | ... | ... |
| (W7′, 0) | ... | 0.33(0.03) | ... |
| (W8′, 0) | 0.6(0.3) | ... | ... |
| (W9′, 0) | 0.9(0.3) | ... | ... |
| (W11′, 0) | 0.8(0.2) | 0.38(0.04) | ... |
| (W12′, 0) | 0.64(0.19) | ... | ... |
| (W13′, 0) | 0.45(0.18) | ... | ... |
| (W14′, 0) | 0.33(0.12) | ... | ... |
| (W15′, 0) | 1.3(0.2) | 0.41(0.03) | ... |
| (W16′, 0) | 1.2(0.3) | ... | ... |
| (W17′, 0) | 0.90(0.19) | ... | ... |
| (W18′, 0) | 0.51(0.14) | ... | ... |
| (W19′, 0) | 0.23(0.14) | ... | ... |

TABLE 2—*Continued*

| Position[b] | Line Intensity[a] ($10^{-5}$ ergs s$^{-1}$ cm$^{-2}$ sr$^{-1}$) $H_2$ $v=$ 1–0 $S(1)$ | $H_2$ $v=$ 2–1 $S(1)$ | $H_2$ $v=$ 6–4 $Q(1)$ |
|---|---|---|---|
| **Orion B/NGC 2023** | | | |
| (0, 0) | 1.82(0.09) | 0.63(0.06) | 0.25(0.06) |
| (0, N160″) | 1.66(0.06) | 0.60(0.04) | 0.70(0.10) |
| (0, S80″) | 3.40(0.06) | 1.38(0.09) | 0.47(0.11) |
| **ρ Oph** | | | |
| (0, 0) | 0.40(0.06) | ... | ... |
| (E3′, 0) | 0.76(0.07) | ... | ... |
| (E6′, 0) | 0.71(0.08) | ... | ... |
| (E9′, 0) | 0.55(0.07) | ... | ... |
| (E12′, 0) | 0.31(0.07) | ... | ... |
| (E15′, 0) | 0.14(0.06) | ... | ... |
| (E18′, 0) | 0.10(0.05) | ... | ... |
| (W3′, 0) | 0.25(0.05) | ... | ... |
| (0, N3′) | 0.29(0.05) | ... | ... |
| (E3′, N3′) | 0.36(0.06) | ... | ... |
| (E6′, N3′) | 0.42(0.07) | ... | ... |
| (E9′, N3′) | 0.42(0.07) | ... | ... |
| (E12′, N3′) | 0.46(0.11) | ... | ... |
| (E3′, 3′ S) | 0.30(0.07) | ... | ... |
| **G236+39** | | | |
| (0, 0) | 0.04(0.05) | ... | ... |

[a] Numbers in parentheses denote 1 $\sigma$ statistical uncertainties.

[b] The position refers to the offset and direction from the source (0, 0) position (see Table 1).

[c] Luhman et al. 1994.

[d] Luhman et al. 1996.

every 10–60 s. We also obtained data near the western edges of the Orion B/NGC 2024 and G236+39 clouds by using the chopping secondary of the CTIO 1.5 m with the reference beam 17′ west of the source. For these cases, the chopper throw was sufficient to avoid source contamination of the sky signal. With the chopping secondary, we fixed the Fabry-Perot etalon at the peak wavelength of the $H_2$ line or at the wavelength of an adjacent continuum channel and chopped the secondary between source and sky at a rate of 0.25–0.5 Hz.

With a 49″ beam, the instrumental velocity resolution was 91 km s$^{-1}$ at 1.60 $\mu$m, 111 km s$^{-1}$ at 2.12 $\mu$m, and 118 km s$^{-1}$ at 2.25 $\mu$m. The resolution decreases with increasing source size. For comparison, for a source that fills the 198″ beam at the McDonald 0.9 m, the velocity resolution at 2.12 $\mu$m is 184 km s$^{-1}$. The flux calibrator for Orion A and B was the B0 Ia star BS 1903 ($m_H = 2.13$, $m_K = 2.18$); for $\rho$ Oph, the M1.5 Ib star BS 6134 ($m_H = -3.21$, $m_K = -3.78$); and for G236+39, the G8 III star BS 3903 ($m_H = 2.12$, $m_K = 2.04$). Based on comparisons with other standard stars, we estimate the relative flux calibration is accurate to $\pm 15\%$.

Table 1 lists the (0, 0) position, sky offset, and beam size for the observations of each source. In Table 2, we list the observed $H_2$ line intensities for each position. The absolute pointing uncertainty is typically 5″. The $H_2$ line intensities in Table 2 are not corrected for line-of-sight extinction. Except for the central region (1′ east–2′ west) in NGC 2024 and the positions in $\rho$ Oph, this correction is not significant. We discuss the extinction toward NGC 2024 in § 3.1 and toward $\rho$ Oph in § 3.2.1.

## 3. RESULTS AND DISCUSSION

### 3.1. $H_2$, $C^+$, *and* CO *in Orion*

In Orion, we observed $H_2$ emission along strip maps across the source. Figures 1 and 2 depict the location of the $H_2$ strip maps together with an outline of the CO emission. In Figures 3–5, we show the corresponding $H_2$ $v = 1$–0 $S(1)$, 2–1 $S(1)$, and 6–4 $Q(1)$ intensity distributions along an east-west strip across the Orion A molecular cloud (Fig. 3*a*), along the Orion A molecular "ridge" (Fig. 4*a*), and along an east-west cut across the NGC 2024/Orion B cloud (Fig. 5*a*). In Figure 3*a*, the distribution of the 1–0 $S(1)$ and 6–4 $Q(1)$ lines are taken from Luhman et al. (1994). For comparison, we also plot the distribution of the [C II] 158 $\mu$m line strength and the $^{12}$CO $J = 1$–0 brightness temperature in Orion A ([C II]—Stacey et al. 1993; Herrmann 1994; Luhman et al. 1996; $^{12}$CO—Schloerb & Loren 1982; Maddalena et al. 1986) and of the [C II] 158 $\mu$m, $^{13}$CO $J = 2$–1, and $^{12}$CO $J = 2$–1 lines in NGC 2024 (Jaffe et al. 1994). All beam sizes are $\sim 1'$, except for the CO data more than 6′ east-west of $\theta^1$ Ori C in Orion A, where the beam size is 2.3 from 6′ to 30′ east-west of $\theta^1$ Ori C and 8.7 farther out.

Beyond the inner 2′–4′ of Orion A, the strength of the $v = 6$–4 $Q(1)$ line ($\sim 3 \times 10^{-6}$ ergs s$^{-1}$ cm$^{-2}$ sr$^{-1}$; $E_{upper} = 3.1 \times 10^4$ K), as well as the ratio of $I_{1-0\ S(1)}$ to $I_{2-1\ S(1)}$ ($\sim 2$), suggests that UV excitation followed by a fluorescent cascade dominates the $H_2$ emission on parsec scales (Black & van Dishoeck 1987; Sternberg 1988). In NGC 2024/Orion B (Fig. 5), the $H_2$ emission extends $\sim 20'$ (2.4 pc) or more from the NGC 2024 H II region/cloud core, and the $H_2$ line ratios also imply that fluorescence dominates the $H_2$ emission. Toward the obscured inner portion of NGC 2024, the visual extinction ranges from 10 to 100 mag (see, e.g., Thompson, Thronson, & Campbell 1981; Thronson et al. 1978, 1984). The high extinction toward the NGC 2024 central region causes the dip in the 1.6 $\mu$m 6–4 $Q(1)$ intensity relative to the $\sim 2.1$ $\mu$m 1–0 $S(1)$ and 2–1 $S(1)$ lines and lowers the absolute peak intensity of the three lines for offset positions (0, 0), (W1′, 0), (W2′, 0), and (E1′, 0).

Within 4′ of $\theta^1$ Ori C, the $H_2$ emission, particularly the 1–0 $S(1)$ line, peaks more sharply than the [C II] and CO intensities (Figs. 3 and 4). Toward the dense ($n \geq 10^5$ cm$^{-3}$) cloud core, intense UV radiation ($\geq 10^5$ times the average interstellar radiation field) from the Trapezium cluster stars heats the gas, allowing collisions to populate the $H_2$ $v = 1$ level and enhance the 1–0 $S(1)$ emission relative to the 2–1 $S(1)$ and 6–4 $Q(1)$ lines (Sternberg & Dalgarno 1989; Burton et al. 1990; Luhman et al. 1996). The powerful molecular outflow emanating from the BN/KL cluster 34″ west and 59″ north of $\theta^1$ Ori C also shock-heats the cloud core within $\sim 1'$ of BN/KL (see, e.g., Gautier et al. 1976; Beckwith et al. 1978; Burton & Puxley 1990). The enhanced 1–0 $S(1)$ emission arising from these thermal-excitation processes explains the narrow 1–0 $S(1)$ emission peak toward the central region. Similarly, excitation of the surrounding

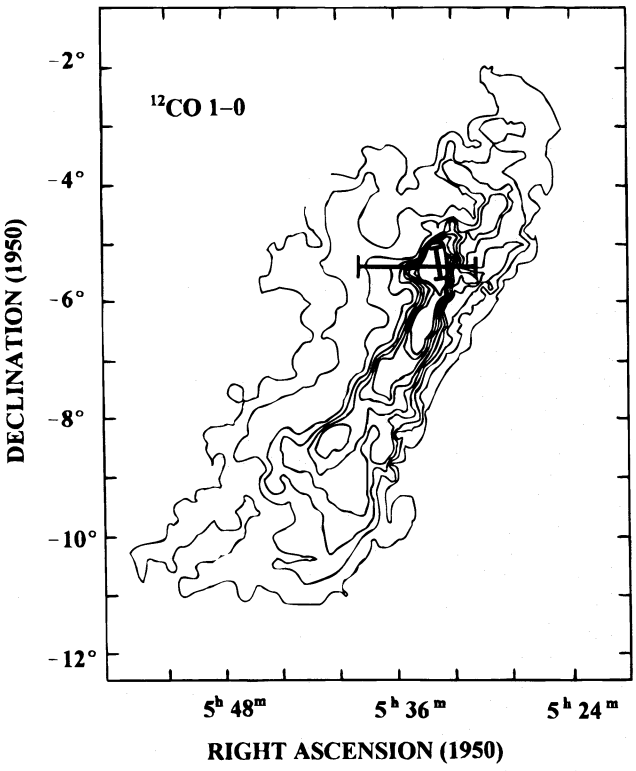


FIG. 1.—Overview of the $^{12}$CO $J = 1$–0 emission from the Orion A molecular cloud complex, adapted from Maddalena et al. (1986). The straight lines mark the orientation, position, and maximum extent of the $H_2$ strip maps of Orion A discussed in § 3.1. The horizontal scan cuts east-west across the cloud, and the second scan lies along the Orion molecular cloud "ridge." The two strip maps intersect at the position of $\theta^1$ Ori C. The $H_2$ intensity distributions along the strips are shown in Figs. 3 and 4.

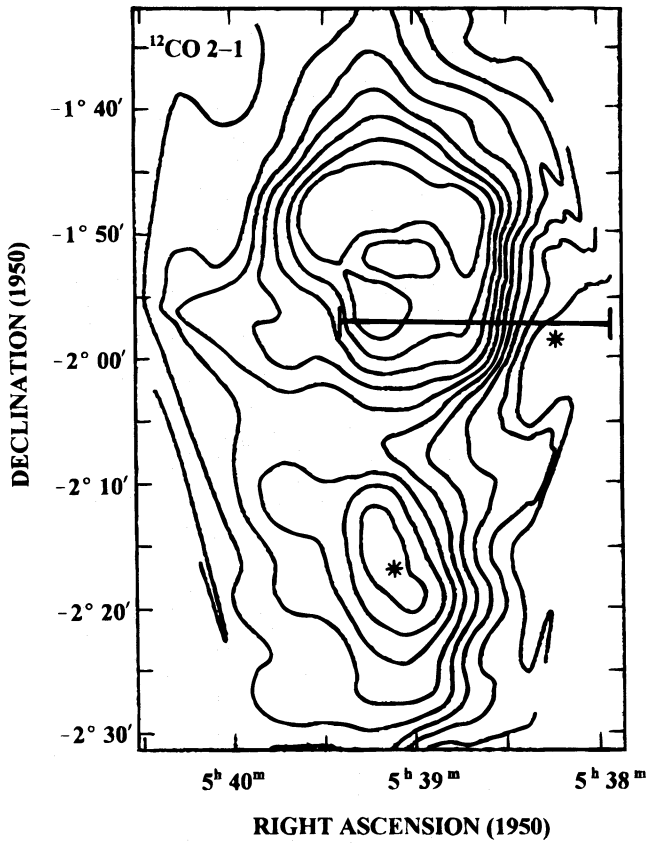


FIG. 2.—Contours of the $^{12}$CO $J = 2$–1 emission from the Orion B molecular cloud, taken from Plume et al. (1996). The northernmost and southernmost emission peaks denote the NGC 2024 and NGC 2023 regions, respectively. The solid line shows the location and extent of the $H_2$ strip map discussed in § 3.1. We show the $H_2$ intensity distribution along the cut in Fig. 5. The asterisks denote the positions of the O star $\zeta$ Ori, near NGC 2024, and the B star HD 37903, near NGC 2023.

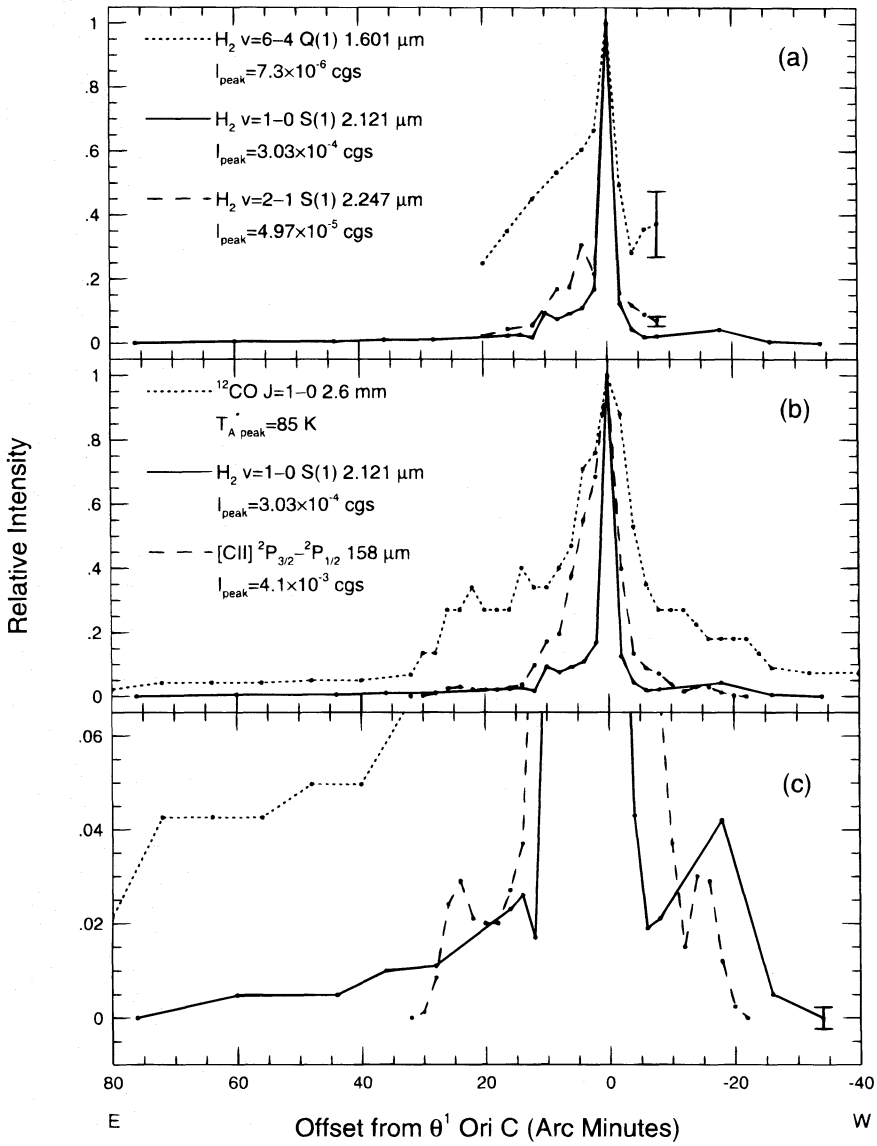


FIG. 3.—(*a*) Right ascension strip map ($\delta_{1950} = -05°25'16''$) across the face of the Orion A molecular cloud in $H_2$ $v = 6$–4 $Q(1)$, $v = 1$–0 $S(1)$, and $v = 2$–1 $S(1)$ (49″ and 65″ beams; see Table 1). The line intensities are normalized by the peak values shown (in ergs $s^{-1}$ $cm^{-2}$ $sr^{-1}$). Typical error bars for the 6–4 $Q(1)$ and 2–1 $S(1)$ intensities are given with the westernmost data points. (*b*) $H_2$ $v = 1$–0 $S(1)$ strip map superposed on cuts of the [C II] 158 $\mu$m line (55″ beam; Stacey et al. 1993) and the $^{12}CO$ $J = 1$–0 line (Schloerb & Loren 1982; Maddalena et al. 1986). The [C II] cut is offset $\sim 75''$ to the north of $\theta^1$ Ori C. The $^{12}CO$ beam size is 50″ within 6′ east-west of $\theta^1$ Ori C. From 6′ to 30′ east-west of $\theta^1$ Ori C, we scaled the 2.′3 resolution $^{12}CO$ brightness temperatures from Schloerb & Loren (1982) to the 50″ data toward the cloud interior. The $^{12}CO$ distribution beyond 30′ east-west is based on the $^{12}CO$ integrated intensities (8.′7 beam) from Maddalena et al. (1986), which we scaled to the Schloerb & Loren data. (*c*) $H_2$ $v = 1$–0 $S(1)$, [C II], and $^{12}CO$ cuts plotted to enhance the low-level emission, showing more clearly the extended (> 10 pc) emission in the 1–0 $S(1)$ line. We show a sample 1–0 $S(1)$ error bar for points that lie more than $\pm 20'$ from $\theta^1$ Ori C. Typical error bars for all other positions are $\sim 4$ (6′–20′ from $\theta^1$ Ori C) or $\sim 10$ (within 6′ of $\theta^1$ Ori C) times larger than the one shown.

molecular material by the OMC-2 outflow source may account for the 1–0 $S(1)$ peak at the 14′ north position along the Orion "ridge" (Fukui et al. 1993). Elsewhere, the $H_2$ line ratios and absolute intensities are consistent with UV fluorescent excitation.

Toward the portions of the Orion A and NGC 2024 clouds where the $H_2$ is purely UV excited, the extended $H_2$ emission falls off much like the [C II] emission and mirrors some of the features of the [C II] distribution. Along the Orion A east-west (Figs. 3*b*, 3*c*) and "ridge" (Fig. 4*b*) cuts, the $H_2$ and [C II] distributions are qualitatively similar, even though along the east-west cut the $H_2$ cut is less well sampled than the [C II] and is offset from the [C II] cut by $\sim 75''$ south. Along the higher angular resolution cut through NGC 2024 (Fig. 5*b*), the similarity between the $H_2$ and [C II] distributions is striking. The $I_{1-0\,S(1)}$-to-$I_{[C\,II]\,158\,\mu m}$ ratio remains basically constant across the cut, with a mean value of $(9.2 \pm 0.5) \times 10^{-3}$ from 3′ east to 14′ west. However, from 15′ to 17′ west of IRS 1 near $\zeta$ Ori, where both $H_2$ and [C II] show a secondary maximum, the $I_{1-0\,S(1)}$-to-$I_{[C\,II]\,158\,\mu m}$ ratio jumps to $\sim 1.6 \times 10^{-2}$. In Orion A, the ratio of $I_{1-0\,S(1)}$ to $I_{[C\,II]\,158\,\mu m}$ in the immediate vicinity of and $\gtrsim 15'$ from the Trapezium cluster is substantially higher ($I_{1-0\,S(1)}/I_{[C\,II]\,158\,\mu m} \sim 0.07$) than in NGC 2024. Toward the Trapezium, the high ratio occurs because both thermal and UV excitation populate the $v = 1$ level of $H_2$ and significantly enhance $I_{1-0\,S(1)}$ relative to $I_{[C\,II]\,158\,\mu m}$ (Luhman et al. 1996). For the Orion A positions $\gtrsim 15'$ from $\theta^1$ Ori C, the gas density falls to below $\sim 3 \times 10^3$ $cm^{-3}$, the critical density of [C II] (Stacey et al. 1993); hence, [C II] drops more rapidly with respect to 1–0 $S(1)$, resulting in high values of $I_{1-0\,S(1)}/I_{[C\,II]\,158\,\mu m}$. The $I_{1-0\,S(1)}$-to-

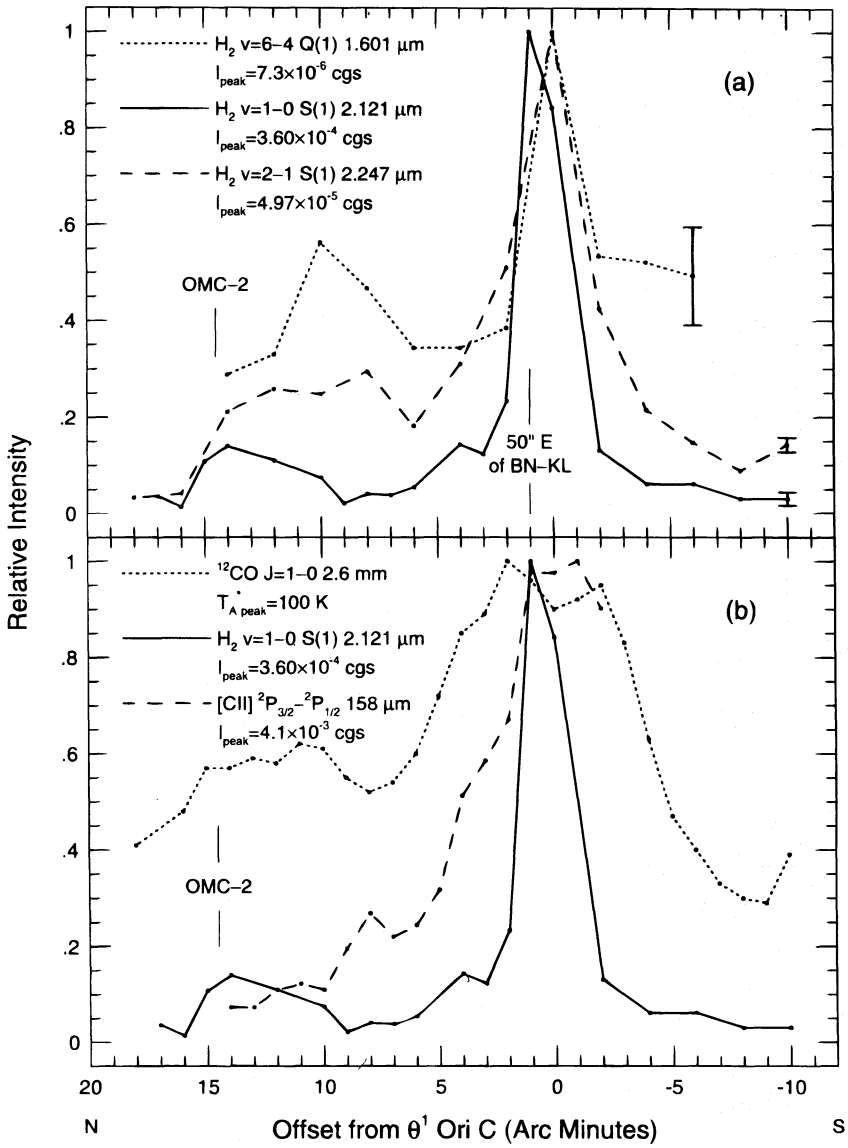


FIG. 4.—(*a*) $H_2$ $v = 6$–4 $Q(1)$, $v = 1$–0 $S(1)$, and $v = 2$–1 $S(1)$ data (49″ beam) cuts along the Orion A molecular "ridge," passing through $\theta^1$ Ori C and OMC-2 (P.A. = 10°.6). The position corresponding to the peak in the 1–0 $S(1)$ emission lies 50″ east of the embedded BN/KL outflow source. Line intensities are normalized by the peak values, shown in cgs units. The southernmost data points display typical uncertainties in the $H_2$ line strengths. (*b*) $H_2$ $v = 1$–0 $S(1)$ strip map shown with the cospatial [C II] 158 $\mu$m (55″ beam; Herrmann 1994; Luhman et al. 1996) and $^{12}$CO $J = 1$–0 (50″ beam; Schloerb & Loren 1982) intensity distributions at 1′ resolution.

$I_{[C\,II]\,158\,\mu m}$ ratios toward intermediate positions that lie ~2′–12′ from the Trapezium are generally consistent with the $I_{1-0\,S(1)}$-to-$I_{[C\,II]\,158\,\mu m}$ ratios in NGC 2024.

In Orion A, all positions where we detect $H_2$ also have significant CO emission. The different beam sizes of the $^{12}$CO 1–0 observations along the Orion A east-west cut (Figs. 3*b*, 3*c*) make it difficult to compare the $H_2$ and $^{12}$CO 1–0 intensity distributions. However, along the Orion A "ridge" (Fig. 4*b*), where the $H_2$ and $^{12}$CO beam sizes are very similar, the low-level 1–0 $S(1)$ emission (more than a few arcminutes north-south of $\theta^1$ Ori C) generally follows the $^{12}$CO 1–0 distribution. In NGC 2024, near $\zeta$ Ori (Fig. 5*d*), a peak in the $^{12}$CO 2–1 (and $^{13}$CO 2–1) intensity distribution coincides with peaks in 1–0 $S(1)$ and [C II]. However, from ~6′ west to ~15′ west of NGC 2024 IRS 1, $I_{1-0\,S(1)}/I_{^{12}CO\,2-1}$ rises by nearly a factor of 20. Over the same region (Fig. 5*d*), $I_{1-0\,S(1)}/I_{^{13}CO\,2-1}$ increases even more dramatically, rising by a factor of 60. (Toward the NGC 2024 H II region, $^{13}$CO 2–1 is more centrally peaked than $H_2$ as a result of a molecular ridge that runs north-south behind the H II region; see, e.g., Schulz et al. 1991; Graf et al. 1993.)

#### 3.1.1. $H_2$ 1–0 $S(1)$ *and* [C II] 158 $\mu$m

Why is there a qualitative similarity between the fluorescent 1–0 $S(1)$ and [C II] emission? When observed on molecular cloud surfaces, the [C II] 158 $\mu$m line traces $T \gtrsim$ 100 K gas, illuminated by 11.2–13.6 eV photons. UV photons that excite $H_2$ in its Lyman and Werner bands also fall in this energy range. Models of PDRs predict that vibrationally excited $H_2$ lies within the $C^+$ layer (e.g., Tielens & Hollenbach 1985a). Thus, the [C II] 158 $\mu$m line and near-IR $H_2$ fluorescent lines should both trace the UV-illuminated boundaries of molecular clouds.

Focusing on the NGC 2024 cut, we can examine the observed $H_2$ and [C II] relationship in more detail. The ratio of the [O I] 63 $\mu$m to [C II] 158 $\mu$m fine-structure line emission from 3′ east to 5′ west along the cut suggests that

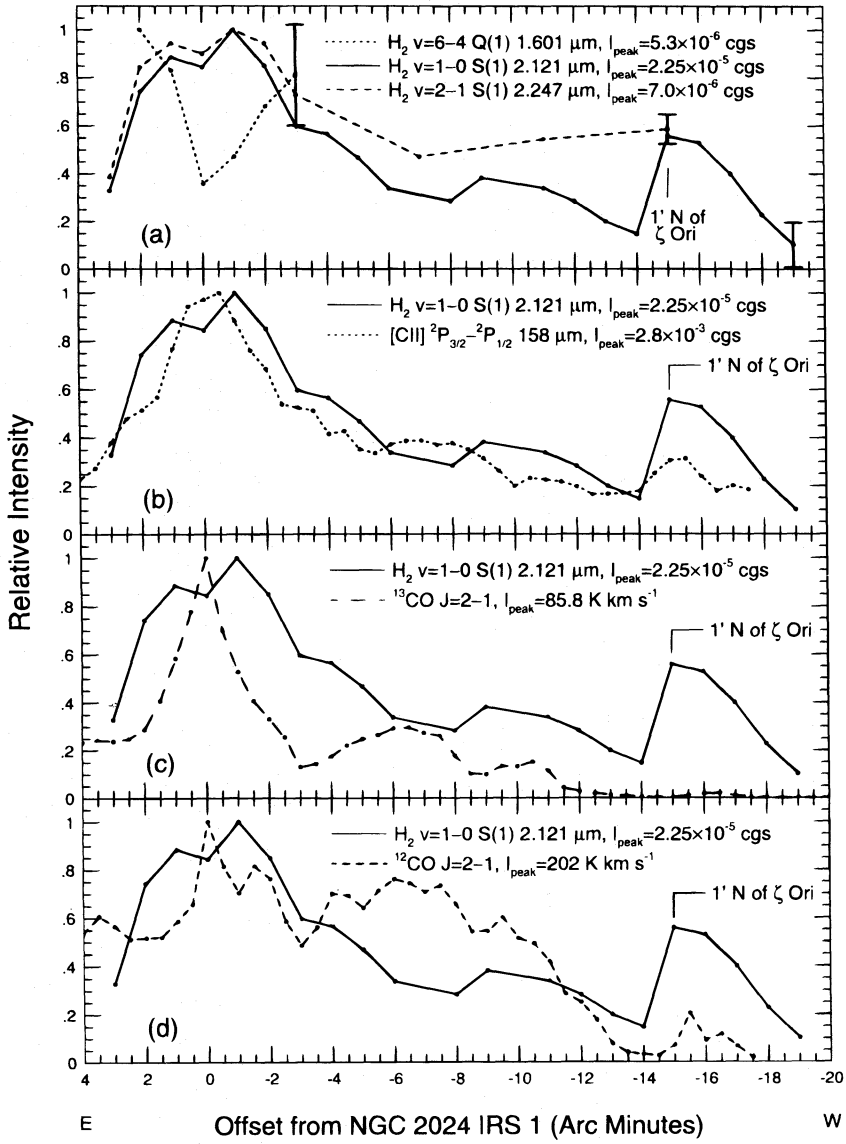


FIG. 5.—(*a*) $H_2$ $v = 6$–4 $Q(1)$, $v = 1$–0 $S(1)$, and $v = 2$–1 $S(1)$ cross-scans along $\delta_{1950} = -01°57'00''$. We obtained the $H_2$ data with a 65″ beam. The peak values along the scans are shown in cgs units. We show sample error bars for each $H_2$ line. The (0, 0) offset position lies in the direction of the star-forming core and the central NGC 2024 H II region. The scan passes 1′ north of ζ Ori (15′ west of NGC 2024 IRS 1) and extends to the western edge of the Orion B cloud as defined by its CO emission (see Fig. 2). We also show comparisons of the $H_2$ 1–0 $S(1)$ distribution with (*b*) [C II] 158 μm, (*c*) $^{13}CO$ $J = 2$–1, and (*d*) $^{12}CO$ $J = 2$–1 (Jaffe et al. 1994). The [C II] beam size is 55″, and the CO beam size is 30″–34″. The $H_2$, [C II], and CO cuts are all cospatial except for the $^{13}CO$ scan from 13′ to 20′ west, which lies 1′ south of the $H_2$ cross-scan.

the gas density $n$ is $\sim 10^4$ cm$^{-3}$ ($I_{[O\,I]\,63\,\mu m}/I_{[C\,II]\,158\,\mu m} =$ 2–3; J. E. Howe 1994, private communication; Jaffe et al. 1994; Luhman et al. 1996). Jaffe et al. (1994) concluded, based on radio and far-IR observations, that the incident UV field strength in NGC 2024 varies from $G \sim 3 \times 10^4$ at the center (toward the peak of the H II region) to $G \sim 300$ at the western ($\sim 15'$ west) CO edge of the cloud, where $G$ is the incident UV intensity measured in units of the equivalent intensity appropriate to the average interstellar medium (ISM) in the solar neighborhood ($1.3 \times 10^{-4}$ ergs s$^{-1}$ cm$^{-2}$ sr$^{-1}$ in the 6–13.6 eV band; Habing 1968). In the wavelength range $\lambda = 91.2$–200 nm, the Habing (1968) field differs by no more than a factor of 2 from the estimates of Jura (1974), Black & Dalgarno (1977), Draine (1978), Gondhalekar, Phillips, & Wilson (1980), and Mathis, Mezger, & Panagia (1983).

Hollenbach, Takahashi, & Tielens (1991, hereafter HTT91) presented one-dimensional theoretical models of low-density ($n = 10^2$–$10^5$ cm$^{-3}$) PDRs exposed to a UV flux. From the HTT91 models, we can derive the emergent intensities of both the [C II] 158 μm and $H_2$ $v = 1$–0 $S(1)$ lines. The [C II] intensities are given directly in Figures 12–14 of HTT91. For $G = 1$–$10^5$ and $n = 10^2$ and $10^4$ cm$^{-3}$, HTT91 plotted the column density of UV-pumped, vibrationally excited $H_2$, $N^*_{H_2}$, which is directly proportional to the total fluorescent $H_2$ emission, $I_{tot}$ ($I_{1-0\,S(1)} \sim 0.018 I_{tot}$; Black & van Dishoeck 1987; Sternberg 1988). For $n$ less than a few times $10^4$ cm$^{-3}$, the UV fluorescence mechanism dominates the excitation of $H_2$ (Luhman et al. 1996). From the HTT91 calculation of $N^*_{H_2}$, we can determine the 1–0 $S(1)$ line strength from

$$I_{1-0\,S(1)} = \frac{1}{4\pi}\left(\frac{N_{v=1,J=3}}{N^*_{H_2}}\right) N^*_{H_2} A_{1-0\,S(1)} h\nu_{1-0\,S(1)} \text{ ergs s}^{-1}\text{ cm}^{-1}\text{ sr}^{-1}, \quad (1)$$

where $N_{v=1,J=3}$ is the column density of the upper state ($v = 1$, $J = 3$) of the 1–0 $S(1)$ transition, $A_{1-0\,S(1)}$ is the quadrupole radiative transition probability for the 1–0 $S(1)$ line ($3.47 \times 10^{-7}$ s$^{-1}$; Turner, Kirby-Docken, & Dalgarno 1977), and $\nu_{1-0\,S(1)}$ is the 1–0 $S(1)$ transition frequency ($1.4139 \times 10^{14}$ Hz). For a range of densities ($n = 10^2$–$10^4$ cm$^{-3}$) and UV field strengths ($G \simeq 1$–$10^4$), Black & van Dishoeck (1987) calculated the fluorescent value of $I_{1-0\,S(1)}$ for a given $N^*_{H_2}$, from which we determine an average value of 0.10 for $N_{v=1,J=3}/N^*_{H_2}$. Using $N^*_{H_2}$ from HTT91 and inserting the above quantities into equation (1), we find that $I_{1-0\,S(1)}$ agrees well with the more detailed calculations of Black & van Dishoeck (1987) and Sternberg (1988).

In Figure 6, we plot the $H_2$ $v = 1$–0 $S(1)$ and [C II] data (*circles*) for the NGC 2024 cut (excluding the positions from 1′ east to 2′ west), along with the model predictions (*crosses*) of HTT91 for $n = 10^4$ cm$^{-3}$ and $G = 10^2$–$(3 \times 10^4)$. A line connecting the models follows the form of the observed relationship between $H_2$ and [C II], but predicts $\sim$2 times higher $H_2$ intensity than we observe. This offset results from the rather arbitrary value of several model parameters (see Appendix A). HTT91 predicted that the [C II] intensity is proportional to $G$ for $G/n \lesssim 1$ cm$^3$ and $n \lesssim 10^4$ cm$^{-3}$ and constant for $G/n \gtrsim 1$ cm$^3$ or when $n \gtrsim 10^4$ cm$^{-3}$ and $G \gtrsim 10^3$. For $n \leq 10^4$–$10^5$ cm$^{-3}$, the UV-excited $H_2$ intensity is proportional to $G$ for $G/n \lesssim 0.02$ cm$^3$ and is proportional to $n$ for $G/n \gtrsim 0.02$ cm$^3$ (Sternberg 1988, 1989; Burton et al. 1990). The behavior of the [C II] and $H_2$ line strengths with $G$ and $n$ results from the competition between dust grains, $H_2$ and CO molecules, and C atoms for the UV photons. The $n = 10^4$ cm$^{-3}$ model points in Figure 6 span the regimes where $G/n \lesssim 0.02$ cm$^3$ ($G \lesssim 3 \times 10^2$) and $G/n \gtrsim 0.02$ cm$^3$ ($G \gtrsim 3 \times 10^2$). The good agreement between the observed $H_2$–[C II] relationship and the modeled behavior implies that the leftmost data points in Figure 6 ($I_{[C\,II]\,158\,\mu m} \lesssim 7 \times 10^{-4}$ ergs s$^{-1}$ cm$^{-2}$ sr$^{-1}$), where the observed 1–0 $S(1)$ intensity declines with decreasing [C II] intensity, are in the regime in which both the 1–0 $S(1)$ and [C II] lines scale with $G$. As this part of the NGC 2024 strip map demonstrates, for the moderate-density ($n \sim 10^4$ cm$^{-3}$), UV-exposed ($G \lesssim 10^3$) gas that characterizes the extended regions of many giant molecular clouds, fluorescent $H_2$ and [C II] emission should vary together with UV field intensity. The flatter dependence of observed $H_2$ intensity on [C II] intensity for $I_{[C\,II]\,158\,\mu m} \gtrsim 10^{-3}$ ergs s$^{-1}$ cm$^{-2}$ sr$^{-1}$ occurs because, at these positions, 1–0 $S(1)$ scales mainly with $n$ while [C II] continues to depend mostly on $G$.

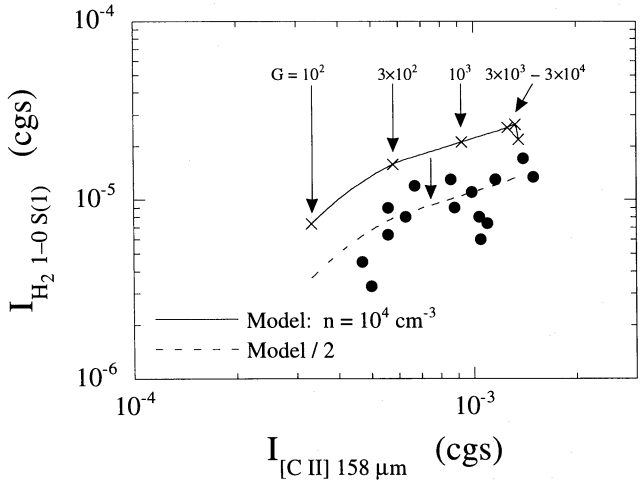


FIG. 6.—Comparison of the observed and theoretical data points relating the $H_2$ $v = 1$–0 $S(1)$ and [C II] 158 $\mu$m emission. We have taken the observed data (*circles*) from the portions of the NGC 2024 cut with low extinction (see text). The crosses represent the predictions of the HTT91 PDR models for gas density $n = 10^4$ cm$^{-3}$ and UV field strength $G = 300$–$(3 \times 10^4)$. The solid line depicts an interpolated fit to the model data. The dashed line shows the model predictions multiplied by 0.5.

In Figure 6, the leftmost data points, where the $H_2$ and [C II] emission vary with UV field strength, generally lie in the outer part (>10′ west) of the NGC 2024 cut. Although changes in UV field strength can explain the relative behavior of the $H_2$ and [C II] emission toward most of the outer NGC 2024 positions, we suspect the 1–0 $S(1)$ dependence on density for $G/n \gtrsim 0.02$ cm$^3$ affects the relative $H_2$–[C II] emission toward a few locations, e.g., the region that extends from 15′ to 17′ west. Here, we see a factor of $\sim$2 increase in the 1–0 $S(1)$ intensity compared to [C II]. Comparison with the $n = 10^4$ cm$^{-3}$ model suggests the 15′ to 17′ west positions fall near $G/n \sim 0.02$ cm$^3$, in which case local density enhancements should increase $I_{1-0\,S(1)}$ relative to $I_{[C\,II]\,158\,\mu m}$. Geometric effects, such as viewing angle or degree of clumpiness of the gas, cannot explain changes in the $H_2$–to–[C II] ratio if both lines are optically thin.

### 3.1.2. *Can UV-excited* $H_2$ *Substitute for* $C^+$ *as a Tracer?*

Our observations demonstrate an excellent spatial correlation between UV-excited $H_2$ and $C^+$, consistent with what one would expect based on models of UV-illuminated molecular clouds. We therefore propose that $H_2$ observations can serve as a substitute for [C II] for tracing the PDR edges of molecular clouds, with several key advantages. Ground-based near-IR $H_2$ observations offer the practical advantage that air-, balloon-, or satellite-borne telescopes are not required. In addition, although the emission from both $H_2$ and $C^+$ behaves similarly for $n \lesssim 10^4$ cm$^{-3}$ and $G \lesssim 10^3$, unlike $C^+$, $H_2$ is not thermally excited. This key difference means that vibrationally excited $H_2$ can effectively trace lower density environments exposed to lower UV radiation fields than can [C II]. The upper state of the [C II] 158 $\mu$m transition is 92 K above ground, and the critical density of the transition is $2.8 \times 10^3$ cm$^{-3}$ for collisions with H and $5 \times 10^3$ cm$^{-3}$ for collisions with $H_2$ (Flower & Launay 1977; Launay & Roueff 1977). Once the kinetic temperature and density of the [C II]–emitting regions fall below these values, the [C II] intensity drops off rapidly with respect to the UV-excited $H_2$ emission. This kind of drop occurs toward the ends of the [C II] east-west cut in Orion A (Figs. 3*b*, 3*c*), where $I_{[C\,II]\,158\,\mu m} \sim (3$–$4) \times 10^{-5}$ ergs s$^{-1}$ cm$^{-2}$ sr$^{-1}$ (Stacey et al. 1993).

Once $I_{[C\,II]\,158\,\mu m}$ falls below $\sim 10^{-5}$ ergs s$^{-1}$ cm$^{-2}$ sr$^{-1}$, other sources besides PDRs can contribute to the diffuse [C II] emission. Fluorescent $H_2$ emission has the advantage that it traces a very specific environment: UV-illuminated molecular surfaces. Observations of [C II] emission probe many phases of the diffuse ISM, including the cold neutral medium, the warm neutral medium, and the warm ionized medium, as demonstrated by a wide variety of recent [C II] observations. Studies by Bock et al. (1993) and Bennett et al. (1994) suggest that the [C II] emission from the diffuse ISM at high Galactic latitudes originates from molecular *and* atomic hydrogen regions. Shibai et al. (1991) and Wright et al. (1991) observed extensive [C II] along the Galactic plane, and toward the Galactic center, Mizutani et al. (1994) detected intense, ubiquitous [C II]. These latter studies

attributed most of the [C II] emission to PDRs on the surfaces of giant molecular clouds, but also argued that extended low-density ionized gas and neutral hydrogen clouds may contribute significantly to the diffuse [C II] emission. From some external galaxies, the photodissociated interfaces of giant molecular clouds dominate the global [C II] intensity (Stacey et al. 1991; Mochizuki et al. 1994). In other galaxies, the ionized medium and neutral atomic clouds may also contribute (Madden et al. 1993). Again, using near-IR $H_2$ observations as a substitute for [C II], we can definitively probe the PDR gas. Given the excellent correlation between fluorescent $H_2$ and [C II] for PDR-dominated sources, large-scale $H_2$ observations can help to disentangle the origin of the [C II] emission toward many UV-exposed environments by tracing the interface between the atomic and molecular medium.

#### 3.1.3. $H_2$ 1–0 $S(1)$ *and* CO

For dense ($n > 10^3$ cm$^{-3}$) clouds near O and B stars, such as Orion A and NGC 2024, PDR interfaces dominate the CO emission (see, e.g., Maloney & Black 1988; Wolfire, Hollenbach, & Tielens 1989; Stacey et al. 1991; Köster et al. 1994). Models of PDRs predict that CO emission arises at $A_V \gtrsim 3$ (e.g., Tielens & Hollenbach 1985a; Burton et al. 1990; HTT91). At this depth, the temperature of the gas is weakly dependent on $G$. Since the $^{12}$CO $J = 1$–0 and $^{12}$CO $J = 2$–1 lines are optically thick, they also have a very weak dependence on $G$. For constant $G$, the intensities of the two $^{12}$CO lines vary with $n$ by no more than a factor of 2 or so for $n > n_{cr}$ (see, e.g., HTT91) where for $^{12}$CO 1–0, $n_{cr} = 3 \times 10^3$ cm$^{-3}$. Along the Orion A east-west cut (Fig. 3*b*), Stacey et al. (1993) suggested that, based on similarities in the spatial extent and distribution of the $^{12}$CO 1–0 and [C II] 158 $\mu$m emission over the inner 6′ of our east-west strip map, the $^{12}$CO 1–0 emission also arises from PDR gas. In Figure 4*b*, the fairly uniform $^{12}$CO 1–0 intensity distribution along the Orion A "ridge," where the density ($n = 10^4$–$10^5$ cm$^{-3}$; Luhman et al. 1996) lies well above the critical density of $^{12}$CO 1–0, is certainly consistent with the PDR behavior we have described.

The general correspondence between the $H_2$ and CO intensity distributions in Orion A is expected if CO really traces molecular gas ($H_2$). However, in NGC 2024, we detect strong $H_2$ emission from sizable portions of the cloud, with weak CO emission. Along the NGC 2024 strip maps (Fig. 5*d*), the $^{12}$CO 2–1 line emission is fairly constant from the eastern edge of the cut to $\sim$6′ west. Over this region, like in Orion A, the $^{12}$CO 2–1 emission behaves in agreement with standard PDR theory. Variations in density and incident UV field strength within a PDR layer at $A_V \gtrsim 3$ cannot explain the rapid decline in the $^{12}$CO 2–1 and $^{13}$CO 2–1 emission relative to $H_2$ westward of the 6′ west offset position. Below, we discuss possible reasons for the decline in $^{12}$CO and $^{13}$CO emission and their ramifications for using $H_2$ as a probe of molecular gas.

#### 3.1.4. *UV-excited* $H_2$: *A Tracer of Molecular Gas with Little* CO

From $\sim$6′ west of the NGC 2024 H II region to the western edge of the NGC 2024 cloud, $I_{[C\ II]\ 158\ \mu m}$ drops from $\sim 1 \times 10^{-3}$ to $\sim 5 \times 10^{-4}$ ergs s$^{-1}$ cm$^{-2}$ sr$^{-1}$ (Jaffe et al. 1994). If we assume that the opacity of the [C II] line is small and $N_{C^+} (= N_{^2P_{3/2}} + N_{^2P_{1/2}}) = 2N_{^2P_{3/2}}$ (a good approximation for $T = 100$–$200$ K and $n \gg 10^3$ cm$^{-3}$), the change in [C II] intensity implies that the beam-averaged $C^+$ column density is $8 \times 10^{17}$ cm$^{-2}$ $\sim$6′ west of IRS 1 and $4 \times 10^{17}$ cm$^{-2}$ at the western edge. For a $C^+$ abundance relative to $H_2$ of $3 \times 10^{-4}$ (i.e., a depletion factor of 0.5), this range of $C^+$ column densities corresponds to an $H_2$ column density $N_{H_2}$ of (1–3) $\times 10^{21}$ cm$^{-2}$. Using the extinction relation of Bohlin, Savage, & Drake (1978), the range of $H_2$ column densities corresponds to $A_V \simeq 1$–3 along the outer portions of the NGC 2024 cut. Thus, toward the extended, western portion of the NGC 2024 cloud, the visual extinction spans a borderline regime where, according to standard PDR theory, we should just begin to see significant CO emission.

Several possible explanations can account for the behavior of the CO lines relative to $H_2$ 1–0 $S(1)$ across the low-$A_V$ ($< 3$) cloud edge of NGC 2024. If the gas in NGC 2024 is clumpy and if the clump sizes increase as one moves east from the western edge, then as $A_V$ increases into the cloud the CO region of each clump becomes larger with respect to $C^+$. For a $C^+$ layer of width comparable to the radius of the clump, the CO emission will increase with clump size compared to the emission from $C^+$ (and $H_2$), even for $\tau_{^{12}CO} > 1$. For a uniform cloud, it is the differences in the photochemistry of $H_2$ and CO as a function of $A_V$ that explain the larger $H_2$-to-CO intensity ratios. As van Dishoeck & Black (1988) discussed in detail, the photodissociation rate of $^{12}$CO and its isotopes depends on cloud depth, as dust particles, $H_2$, C, and CO attenuate the supply of UV photons. For example, van Dishoeck & Black showed that, for a UV-illuminated ($G \sim 30$), dense ($n \sim 10^4$ cm$^{-3}$) cloud, the CO photodissociation rate drops by an order of magnitude from the cloud edge ($A_V \leq 1$) to 0.3–0.4 pc ($A_V \sim 3$) inward from the surface. The $H_2$ photodissociation rate is also a function of depth, but because in part of the much larger abundance of $H_2$, self-shielding of $H_2$ becomes important at much smaller depths than CO self-shielding. As discussed in § 3.1.1, the ratio of UV field intensity $G$ to density $n$ is $\lesssim 0.02$ cm$^3$ toward the western edge of NGC 2024. Self-shielding of $H_2$ begins near this $G/n$ regime (Burton et al. 1990). As the detailed PDR models demonstrate, one therefore should expect a low column density molecular cloud to have $H_2$ but no CO. As the thickness of the cloud increases, a CO/$H_2$ layer appears behind the $C^+$/$H_2$ and $C^0$/$H_2$ layers.

Because of differences in the abundances and photodissociation rates of CO and $H_2$, significant column densities of $H_2$ can exist along UV-exposed boundaries where the CO column density is small. From the discussion above, we contend that the western edge of NGC 2024 is an example of such an environment, where $N_{H_2} = (1$–$3) \times 10^{21}$ cm$^{-2}$ in a region with little CO emission. If the $H_2$-CO emission in NGC 2024 is typical of low-$A_V$ environments exposed to moderate ($G \gtrsim 100$) UV fields, observations of the surfaces of many giant molecular clouds are likely to show fluorescent $H_2$ emission in regions devoid of CO. As Plume et al. (1996) pointed out, for clouds with $A_V \sim 8$ from the surface to the interior, as much as half the carbon is in the form of C and $C^+$ as opposed to CO. Thus, even for environments with moderate $A_V$, much of the material can reside in regions with no CO. Observations of UV-excited $H_2$ provide a way to detect molecular gas along cloud boundaries where the CO emission suggests that little molecular material exists. This effect should be even more extreme in low-metallicity environments such as the interstellar media of the Large and Small Magellanic Clouds. Other possible sites for the detection of molecular gas via

$H_2$ where little CO is present are diffuse, low column density clouds, such as the CO-poor clouds detected by Lada & Blitz (1988) and interstellar cirrus clouds such as the G236+39 cloud observed in this study (see, e.g., Blitz, Bazell, & Désert 1990; Reach et al. 1994).

### 3.2. *Correlation between* $H_2$ *and the Far-IR Continuum*

#### 3.2.1. $H_2$ 1–0 *S*(1) *and* $I_{60\,\mu m}$ *and* $I_{100\,\mu m}$

In Figures 7 and 8, we plot the observed $H_2$ $v = 1$–0 $S(1)$ intensity (*circles, diamonds*) for all positions where fluorescence dominates the $H_2$ emission, as a function of the 60 and 100 $\mu$m continuum emission from dust as measured by *IRAS*. For bright ($I_{1-0\,S(1)} \gtrsim 10^{-5}$ ergs s$^{-1}$ cm$^{-2}$ sr$^{-1}$) positions, we generally have observations of more than one $H_2$ line (except for some positions along the Orion "ridge"). For these positions, we determined whether the position was fluorescent from the $H_2$ line ratios, e.g., $I_{1-0\,S(1)}/I_{2-1\,S(1)} \sim 2$ (Black & van Dishoeck 1987; Sternberg 1988). For the fainter positions, where we observe the 1–0 $S(1)$ line only, we assume that the $H_2$ emission is fluorescent. We exclude from our analysis the obscured positions toward NGC 2024 at (0, 0), (W1′, 0), (W2′, 0), and (E1′, 0). We obtained 60 and 100 $\mu$m maps of the observed regions from the *IRAS* Sky Survey Atlas, to which we applied no additional deconvolution or smoothing. Using the Orion and NGC 2024 data, but not the data for $\rho$ Oph (*diamonds*) or G236+39 (upper limit), we fitted a power law ($I_{H_2} \propto I_{FIR}^{\alpha}$; *solid line*) to the $H_2$ and far-IR data. The 1–0 $S(1)$ data in Figures 7 and 8 have not been corrected for extinction, except at the positions in $\rho$ Oph, which is the only region included in the figures where $A_K$ may be greater than 1 mag. To deredden the $\rho$ Oph data, we adopted the visual extinction as measured by Elias (1978) toward the nearest associated star, either HD 147889 ($A_V = 4.6$), S1 ($A_V = 12.5$), or SR 3 ($A_V = 6.2$), and applied the Rieke & Lebofsky (1985) extinction curve ($A_K = 0.112 A_V$). Once dereddened, the 1–0 $S(1)$ data for $\rho$ Oph are consistent with the power-law fit to the Orion 1–0 $S(1)$ and far-IR data.

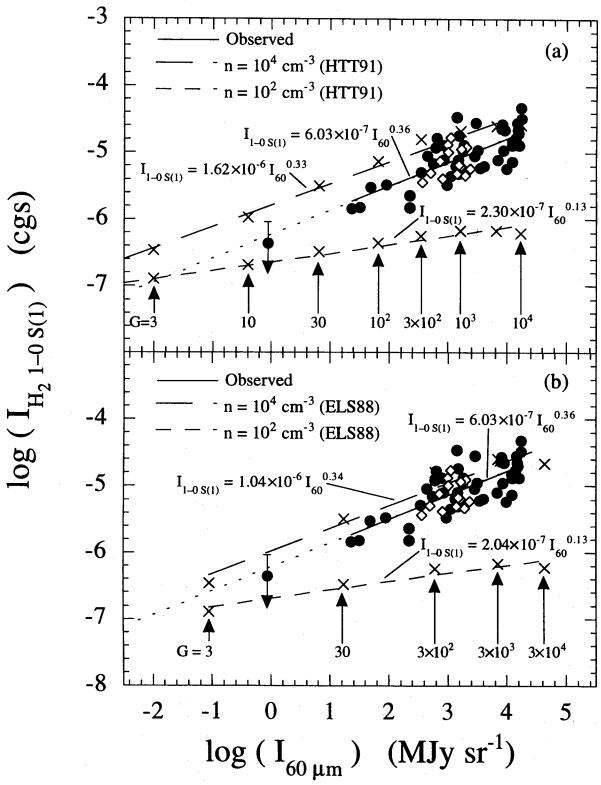


FIG. 7.—(*a*) Correlation of $H_2$ $v = 1$–0 $S(1)$ line intensity with 60 $\mu$m continuum intensity across the UV-illuminated surfaces of Orion A and B (*circles*), $\rho$ Oph (*diamonds*), and G236+39 (*circle*; upper limit). The solid line is a least-squares fit through the observed points, leaving out the upper limit at the left. The crosses represent the predictions for the $H_2$ and 60 $\mu$m intensities given by the HTT91 PDR models. The figure shows two families of models, one for a cloud edge with a uniform density $n = 10^4$ cm$^{-3}$ and one with $n = 10^2$ cm$^{-3}$. The assumed UV field intensity $G$ of each model data point is labeled. As with the observations, we fitted power laws (*long- and short-dashed lines*) to the model results. (*b*) Comparison of the observed and calculated correlations between $I_{1-0\,S(1)}$ and $I_{60\,\mu m}$, where we have calculated $I_{60\,\mu m}$ using the ELS88 dust code. As in the top panel, for the $G$ that corresponds to the 60 $\mu$m intensity, we derived the 1–0 $S(1)$ line strength from the column density of excited $H_2$ calculated by HTT91.

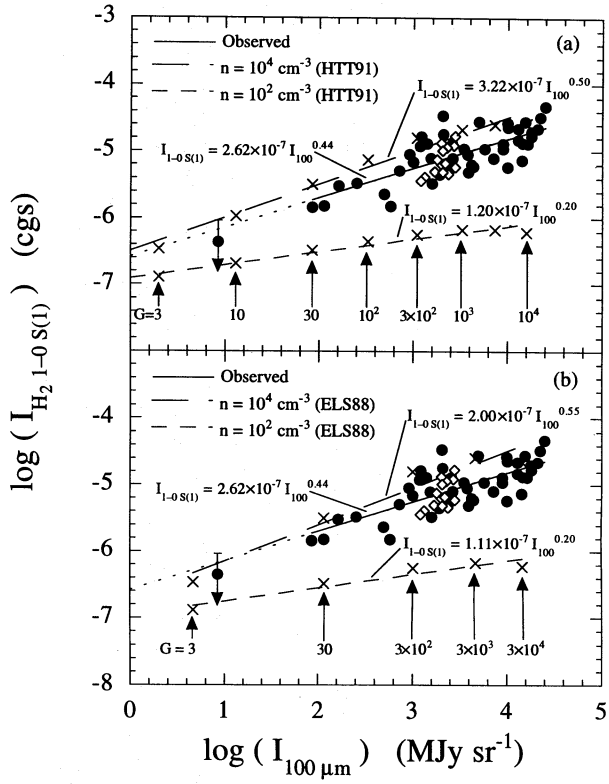


FIG. 8.—Same as Fig. 7, but for the 100 $\mu$m continuum intensity

How do we explain the correlation of the 1–0 $S(1)$ line and the far-IR continuum intensities? From the power-law indices $\alpha$ of the fits to the $H_2$ and far-IR data in Figures 7 and 8 ($\alpha_{60\,\mu m} = 0.36$ and $\alpha_{100\,\mu m} = 0.44$), we can immediately rule out a surface area/volume ratio geometric effect as the sole explanation of the observed dependence. If, for each line of sight, the $H_2$ and far-IR emission were dominated by a region with an effective radius $R_{eff}$, where the $H_2$ emission $I_{H_2}$ originated from the cloud surface ($I_{H_2} \propto R_{eff}^2$) and the far-IR radiation $I_{FIR}$ came from the bulk of the cloud ($I_{FIR} \propto R_{eff}^3$), we would expect $I_{H_2} \propto I_{FIR}^{2/3}$. Thus, a surface area/volume ratio effect would yield a steeper power-law fit than we observe. Since all of the sources are well resolved, aperture effects also cannot explain the correlation.

Except for the small fraction of the UV radiation used to excite $H_2$, essentially all of the incident radiation field heats the dust in the cloud surface layers and reemerges in the far-IR. Therefore, in Figures 7 and 8, we also plot theoretical data (*crosses*) that assume that both the $H_2$ and dust emission arise from the surface of a UV-illuminated cloud.

For a given UV field intensity $G$, HTT91 calculated the fraction of the far-IR emission that emerges at 60 and 100 $\mu$m by assuming that the surface ($A_V \leq 1$) layer produces optically thin far-IR radiation. The strength of the UV flux $G$ dictates the dust temperature $T_{dust}$ ($\propto G^{0.2}$), and from the temperature of the dust in the cloud, HTT91 calculated the far-IR radiation assuming that the flux incident on the surface equals the outgoing flux of dust radiation. The parameter space studied by HTT91 spans the range of excitation conditions that characterize the observed environments plotted in Figures 7 and 8. From the HTT91 calculations of $N^*_{H_2}$, we determined the fluorescent 1–0 $S(1)$ line strength as outlined in § 3.1.1. In Figures 7*a* and 8*a*, we plot the 1–0 $S(1)$ and far-IR model results from HTT91 for $n = 10^2$ cm$^{-3}$ and $10^4$ cm$^{-3}$ for various values of $G$.

The ratio of the far-IR intensities at 60 and 100 $\mu$m derived from the HTT91 models is a very sensitive function of $T_{dust}$. For $G = 1$–$10^4$, $T_{dust}$ ranges from $\sim$10 K to $\sim$80 K, which corresponds to a range of 0.02–3 (more than 2 orders of magnitude) in $I_{60}/I_{100}$. To test whether the predicted far-IR intensity ratios depend strictly on the model-specific treatment of $T_{dust}$ and other parameters, such as the dust properties, we attempted to reproduce the HTT91 far-IR results using the dust code of Egan, Leung, & Spagna (1988, hereafter ELS88). The ELS88 results are shown in Figures 7*b* and 8*b*. This code solves the radiative transfer problem for a spherically symmetric dust envelope illuminated by a central heat source. The code treats the radiative transfer problem as a two-point boundary-value problem, taking into account the effects of multiple scattering, absorption, and reemission of photons. We discuss the input parameters for the ELS88 code in Appendix B. Since the ELS88 models do not treat the $H_2$ emission, we adopted the $H_2$ results from HTT91 for the model plots in both the upper and lower panels of Figures 7 and 8. As with the observed data, we fitted power laws to the HTT91 and ELS88 model data. For both the 60 and 100 $\mu$m results, we see that the $n = 10^4$ cm$^{-3}$ fit (*long-dashed line*) for both HTT91 and ELS88 closely matches the observed behavior, with a slight offset in the $H_2$ intensity at a given far-IR intensity (see Appendix A).

The slope and position of the $I_{1-0\,S(1)}$–$I_{FIR}$ relation in Figures 7 and 8 implies that the gas density is moderately high at the surface where UV strikes the Orion and $\rho$ Oph clouds. The models for $n = 10^2$ cm$^{-3}$ lie well below the observations and have a much flatter slope. Densities much in excess of $10^4$ cm$^{-3}$ would lead to collisional excitation of the $v = 1$ level of $H_2$ and would raise the observed data significantly above the $n = 10^4$ cm$^{-3}$ model fit (Luhman et al. 1996). Thus, the gas density of the surface(s) of the clouds likely ranges from a few thousand to $10^4$ cm$^{-3}$. This estimate agrees with previous cospatial observations of the [O I] 63 $\mu$m and [C II] 158 $\mu$m line emission from Orion A and B (Luhman et al. 1996).

#### 3.2.2. *The Far-IR Continuum: A Good Measure of Cloud Mass?*

The similarity between the $n = 10^4$ cm$^{-3}$ models and the observations suggests that we can explain the observed correlation between the 1–0 $S(1)$ and far-IR emission solely in terms of their mutual dependence on the intensity of the UV field, with the $H_2$ and dust emission both originating primarily from the UV-exposed surface layers of the cloud. If both the $H_2$ *and* far-IR radiation arise in PDRs, in environments like the Orion and $\rho$ Oph cloud complexes, which have nearby O and B stars to heat the dust, the far-IR continuum emission comes from a constant-$A_V$ ($\sim$0.5–1) region at the cloud surface. Thus, the optical depth of the far-IR continuum is not the optical depth through the entire cloud, but rather the optical depth of that portion of the cloud envelope where most of the UV photons are consumed. Often, one uses the far-IR surface brightness to infer a gas column density and the mass of the cloud (e.g., Boulanger & Perault 1988; Heiles, Reach, & Koo 1988; Reach et al. 1994). If the large-scale far-IR emission traces mainly the PDR interface, the far-IR surface brightness emission will not reliably trace the total gas mass. Therefore, near OB-star–forming regions and in the central regions of luminous galaxies, the use of the far-IR continuum emission as a probe of cloud mass should be questioned.

For well-resolved regions such as giant molecular clouds, the far-IR continuum flux, together with the 1–0 $S(1)$ emission, can provide a rough measure of the surface density and incident UV field intensity, as shown in Figures 7 and 8. However, given the sizable dispersion of the data points, we caution against using a measurement of the 1–0 $S(1)$ and far-IR emission toward a single position as a diagnostic of the cloud surface conditions. Given the relationship between the 1–0 $S(1)$ and far-IR emission, we can also use the far-IR flux to deredden the 1–0 $S(1)$ emission toward heavily obscured environments. The agreement between the dereddened $\rho$ Oph 1–0 $S(1)$ data (*diamonds*, Figs. 7 and 8) and the other data provides evidence of the feasibility of this approach.

#### 3.2.3. *Other $H_2$ Lines and $I_{60\,\mu m}$ and $I_{100\,\mu m}$*

In the fluorescent-excitation regime, the relative intensities of the $H_2$ lines scale by a constant factor, which depends on the branching ratios of the radiative transitions (Black & van Dishoeck 1987; Sternberg 1988). Thus, we can predict in a straightforward way the relationship between $I_{60\,\mu m}$ and $I_{100\,\mu m}$ and any fluorescing $H_2$ line from the power-law fit of $I_{1-0\,S(1)}$ versus $I_{60\,\mu m}$ and $I_{100\,\mu m}$. We can examine our observations of the 2.247 $\mu$m $v = 2$–1 $S(1)$ and 1.601 $\mu$m $v = 6$–4 $Q(1)$ lines to test the thesis that their intensities should obey the $I_{1-0\,S(1)}$-versus-$I_{FIR}$ scaling law. According to Black & van Dishoeck (1987) and Sternberg (1988), the ratios of the 2–1 $S(1)$ and 6–4 $Q(1)$ lines to the 1–0 $S(1)$ line are $\sim$0.53 and $\sim$0.34, respectively.

Scaling the empirical 1–0 $S(1)$ power laws in Figure 8 by 0.53 and 0.34, we plot in Figure 9 the expected fluorescent power-law relationship (*dashed line*) between 2–1 $S(1)$ and $I_{100\,\mu m}$ (Fig. 9*a*) and 6–4 $Q(1)$ and $I_{100\,\mu m}$ (Fig. 9*b*). In Figure 9, we also plot our 2–1 $S(1)$ and 6–4 $Q(1)$ data and a power-law fit to the observations (*solid line*). In Figure 9*a*, we see excellent agreement between the predicted "pure" radiative fluorescent ($\alpha_{100\,\mu m} = 0.44$) and observed ($\alpha_{100\,\mu m} = 0.42$) indices for the 2–1 $S(1)$ line. The absolute intensity scaling of the 2–1 $S(1)$ line is also consistent with "pure" $H_2$ fluorescence. The observed power-law index $\alpha$ for the 6–4 $Q(1)$ transition is 0.06 for the 100 $\mu$m case. This relation is significantly flatter than the index derived from the 1–0 $S(1)$ observations under the assumption of radiative fluorescence. The flatter empirical fit suggests that in the high-$G$ ($>10^3$) case for $n \sim 10^4$ cm$^{-3}$, i.e., the regime that describes the data points on the right-hand side of Figure 9*b*, collisional de-excitation of the high-$v$ ($>2$) states of $H_2$ suppresses the 6–4 $Q(1)$ line strength. This result agrees with our recent study (Luhman et al. 1996), which showed that, for $n$ of a few times $10^4$ cm$^{-3}$, collisional de-excitation sig-

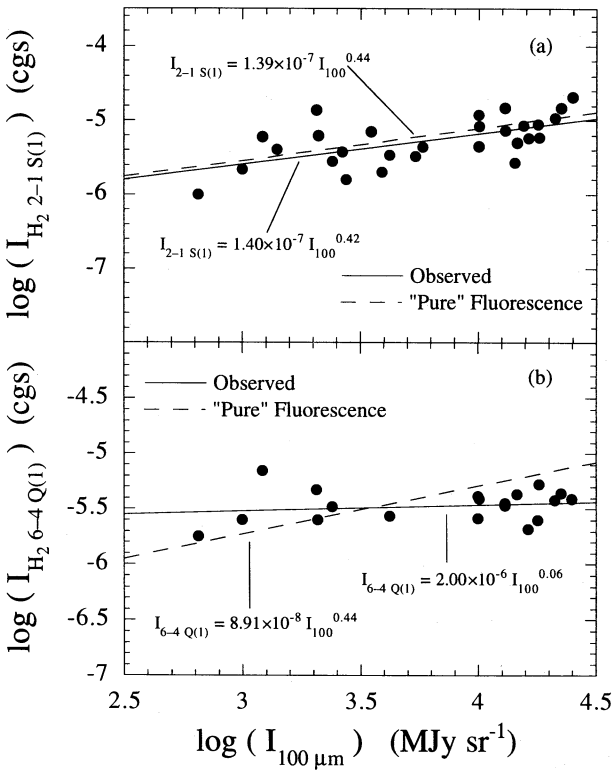


FIG. 9.—(*a*) $H_2$ $v = 2$–1 $S(1)$ observed line strength (*circles*) plotted against the 100 $\mu$m continuum emission for the source positions in Table 2. The solid line represents a least-squares fit to the data. For comparison, we plot the expected behavior (*dashed line*) of the 2–1 $S(1)$ line implied by the observed relationship between $I_{1-0\ S(1)}$ and $I_{100\ \mu m}$ (see Fig. 8) and assuming "pure" radiative fluorescent emission of the 1–0 $S(1)$ line, i.e., $I_{2-1\ S(1)} \simeq 0.53 I_{1-0\ S(1)}$. (*b*) Observed correlation (*solid line*) of the $H_2$ $v = 6$–4 $Q(1)$ and 100 $\mu$m emission (*circles*), compared with the relationship (*dashed line*) implied by the 1–0 $S(1)$ correlation (Fig. 8) if we assume "pure" radiative fluorescent 1–0 $S(1)$ emission, i.e., $I_{6-4\ Q(1)} \simeq 0.34 I_{1-0\ S(1)}$.

nificantly affects the 6–4 $Q(1)$ line intensity relative to the 2–1 $S(1)$ and the 1–0 $S(1)$ emission. The 6–4 $Q(1)$ transition is therefore more responsive to collisional effects than the 2–1 $S(1)$ and 1–0 $S(1)$ transitions. This result implies that with respect to the far-IR continuum emission, the high-$v$ ($v > 2$) line emission exhibits less dynamic range than the low-$v$ emission. For the range of $I_{100\ \mu m}$ plotted in Figure 9, $I_{6-4\ Q(1)}$ may therefore provide a measure of area filling factor.

## 4. SUMMARY

We have studied the near-IR $H_2$ emission from the UV-exposed surfaces of a sample of galactic clouds. The observed surfaces generally reside well outside highly energetic environments, such as star-forming cores, and emit diffuse ($< 10^{-5}$ ergs s$^{-1}$ cm$^{-2}$ sr$^{-1}$) near-IR $H_2$ line radiation that arises from UV excitation (UV fluorescence). We find that the $H_2$ emission correlates well with [C II] 158 $\mu$m and the far-IR continuum radiation from dust grains. In some cases, such as along the Orion A molecular "ridge," the $H_2$ emission also follows CO. These correlations suggest that, like $H_2$, emission from $C^+$, CO, and dust particles along the UV-irradiated surfaces dominates the total emission from the cloud. For some photon-dominated environments, such as toward the western edge of the Orion B/NGC 2024 cloud, the UV flux dissociates CO in regions where the $H_2$ emission persists.

The observed correlations, or lack thereof, between $H_2$ and $C^+$, CO, and the far-IR continuum demonstrate the following: (1) $H_2$ can trace many of the same photon-dominated regions as $C^+$, down to low densities and incident UV field strengths at which [C II] emission from neutral and ionized atomic hydrogen regions has surface brightnesses comparable to PDRs; (2) $H_2$ is a definitive tracer of molecular gas in regions where emission from $C^+$ can arise from neutral or ionized material or where UV photons dissociate CO along cloud edges; and (3) for clouds exposed to UV radiation from nearby early-type stars, the large-scale far-IR emission, like $H_2$, probes the surface of the cloud, not the cloud's interior, and thus is a dubious tracer of cloud column density.

The authors would like to thank Soojong Pak and L. D. Keller for their assistance on observing runs. We would also like to thank H. L. Dinerstein, T. R. Geballe, J. H. Lacy, and the anonymous referee for many useful suggestions which improved this paper. This work was supported by NSF grant AST 91-17373, the David and Lucile Packard Foundation through a fellowship to D. T. J., and NASA Graduate Traineeship grant NGT-50998, held by M. L. L.

## APPENDIX A

## OBSERVATIONS AND HTT91 MODELS

In Figures 6–8, the observed $H_2$ 1–0 $S(1)$ intensity is slightly offset from the HTT91 model predictions. For the $n = 10^4$ cm$^{-3}$ model, the observed $H_2$ intensity departs by roughly a factor of 2 from the model calculations. An explanation for this offset lies in one of two areas:

1. Reasonable changes in several HTT91 model parameters, such as the grain properties and the gas temperature, can yield lower values of $I_{1-0\ S(1)}$ for the same $n$ and $G$ (see, e.g., Tielens & Hollenbach 1985a; Black & van Dishoeck 1987). The value of the total fluorescent $H_2$ emission, $I_{tot}$, depends on the competition between grains and $H_2$ molecules for the available UV photons. Thus, a larger adopted value of the effective grain–continuum UV absorption cross section $\sigma$ (cm$^2$), for example, implies $H_2$ competes less effectively with the dust for $H_2$ pumping photons and decreases $I_{tot}$. Since dust grains serve as formation sites of interstellar $H_2$ (Jura 1974), a decrease in the model gas-to-dust ratio and/or the efficiency with which molecules form per atom-grain collision decreases the $H_2$ formation rate and reduces $I_{tot}$ (Hollenbach & Salpeter 1971; Hollenbach, Werner, & Salpeter 1971). Likewise, decreasing the gas temperature decreases the atom-grain collision frequency, which again decreases the $H_2$ formation rate and therefore also $I_{tot}$. Such changes in the model parameters can easily lower $I_{1-0\ S(1)}$ by the factor of 2 required to match the observations.

2. The actual gas density at the cloud surface could be slightly less than $10^4$ cm$^{-3}$. As illustrated in Figures 7 and 8, increasing the model gas density increases the calculated 1–0 $S(1)$ emission. Thus, the model data for, say, $n = 5 \times 10^3$ cm$^{-3}$ could lie closer to the observed data, but with a flatter power-law fit than predicted for $n = 10^4$ cm$^{-3}$. The flatter fit would better match the observations for the $H_2$–versus–100 $\mu$m correlation but would worsen the agreement with the observed $H_2$–versus–60 $\mu$m relation.

## APPENDIX B

## ELS88 DUST CODE

The ELS88 dust code requires the following input parameters: (1) the stellar radiation field, parameterized by the stellar luminosity, $L_*$, and temperature, $T_*$; (2) the inner and outer radii of the spherical cloud ($r_i$ and $r_o$, respectively); (3) the density profile between $r_i$ and $r_o$, described by a power law $n(r) \propto n_i(r/r_i)^{-\alpha}$, where $n_i$ is the density at $r_i$; (4) the dust properties, parameterized by the dust absorption and scattering efficiency at each frequency; and (5) the 100 $\mu$m optical depth, $\tau_{100\mu m}$. The output includes the grain temperature distribution throughout the envelope and the integrated surface brightness at each of 60 wavelengths, including 60 and 100 $\mu$m.

For the central source of UV photons, we chose a B2 star with $T_* = 22{,}000$ K, although the results are very insensitive to $T_*$. We varied $L_*$ to produce a UV flux ranging from $G = 3$ to $G = 3 \times 10^4$ incident on the inner surface of the envelope, where $r_i = 1$ pc and $r_o = 1.01$ pc. We chose a constant ($\alpha = 0$) density profile. We specified a 100 $\mu$m optical depth $\tau_{100\,\mu m} = 0.001$, consistent with the optically thin HTT91 treatment. The shell geometry of ELS88 does not affect the emergent optically thin far-IR radiation compared to the plane-parallel slab geometry of HTT91. We adopted the dust properties given by Draine & Lee (1984).

We compared far-IR fluxes obtained with the Draine & Lee dust opacities to those obtained using the opacity law of Mathis et al. (1983) and found that, for $G = 30$ to $G = 3 \times 10^4$, the relative variations in the 60 and 100 $\mu$m emission with respect to the 1–0 $S(1)$ intensity are virtually identical, although, depending on $G$, $I_{FIR}$ obtained with Mathis et al. opacities is typically 2–6 times smaller than $I_{FIR}$ with the Draine & Lee opacity law for our models. For low $G$ ($< 100$), the calculated dust temperature is sufficiently cold that the 60 and 100 $\mu$m emission lies on the Wien side of the blackbody curve. In this regime, the far-IR model calculations are especially sensitive to the adopted dust-grain model.

## REFERENCES


Anthony-Twarog, B. J. 1982, AJ, 87, 1213
Beckwith, S., Evans, N. J., II, Gatley, I., Gull, G., & Russell, R. W. 1983, ApJ, 264, 152
Beckwith, S., Persson, S. E., Neugebauer, G., & Becklin, E. E. 1978, Ap$^1$, 223, 464
Bennett, C. L., et al. 1994, ApJ, 434, 587
Black, J. H., & Dalgarno, A. 1976, ApJ, 203, 132
———. 1977, ApJS, 34, 405
Black, J. H., & van Dishoeck, E. F. 1987, ApJ, 322, 412
Blitz, L., Bazell, D., & Désert, F.-X. 1990, ApJ, 352, L13
Bock, J., et al. 1993, ApJ, 410, L115
Bohlin, R. C., Savage, B. D., & Drake, J. F. 1978, ApJ, 224, 132
Boulanger, F., & Perault, M. 1988, ApJ, 330, 964
Burton, M. G., Hollenbach, D. J., & Tielens, A. G. G. M. 1990, ApJ, 365, 620
Burton, M. G., & Puxley, P. 1990, in The Interstellar Medium in External Galaxies, ed. D. J. Hollenbach & H. A. Thronson, Jr. (NASA CP-3084) (Washington, DC: NASA), 238
Dalgarno, A. 1992, in IAU Symp. 150, Astrochemistry of Cosmic Phenomena, ed. P. D. Singh (Dordrecht: Kluwer), 2
de Boer, K. S. 1983, A&A, 125, 258
de Jong, T., Dalgarno, A., & Boland, W. 1980, A&A, 91, 68
Dinerstein, H. L., Lester, D. F., Carr, J. S., & Harvey, P. M. 1988, ApJ, 327, L27
Draine, B. T. 1978, ApJS, 36, 595
Draine, B. T., & Lee, H. M. 1984, ApJ, 285, 89
Egan, M. P., Leung, C. M., & Spagna, G. F., Jr. 1988, Comput. Phys. Commun., 48, 271 (ELS88)
Elias, J. H. 1978, ApJ, 224, 453
Flower, D. R., & Launay, J. M. 1977, J. Phys. B, 10, 3673
Fukui, Y., Iwata, T., Mizuno, A., Bally, J., & Lane, A. P. 1993, in Protostars and Planets III, ed. E. H. Levy & J. I. Lunine (Tucson: Univ. Arizona Press), 603
Gatley, I., et al. 1987, ApJ, 318, L73
Gatley, I., & Kaifu, N. 1987, in IAU Symp. 120, Astrochemistry, ed. M. S. Vardya & S. P. Tarafdar (Dordrecht: Reidel), 153
Gautier, T. N., Fink, U., Treffers, R. R., & Larson, H. P. 1976, ApJ, 207, L129
Genzel, R., & Stutzki, R. 1989, ARA&A, 27, 41
Gondhalekar, P. M., Phillips, A. P., & Wilson, R. 1980, A&A, 85, 272
Graf, U. U., Eckart, A., Genzel, R., Harris, A. I., Poglitsch, A., Russell, A. P. G., & Stutzki, J. 1993, ApJ, 405, 249
Habing, H. J. 1968, Bull. Astron. Inst. Netherlands, 19, 421
Hasegawa, T., Gatley, I., Garden, R. P., Brand, P. W. J. L., Ohishi, M., Hayashi, M., & Kaifu, N. 1987, ApJ, 318, L77
Hayashi, M., Hasegawa, T., Gatley, I., Garden, R., & Kaifu, N. 1985, MNRAS, 215, 31P
Heiles, C., Reach, W. T., & Koo, B.-C. 1988, ApJ, 332, 313
Herrmann, F. 1994, Ph.D. thesis, Ludwig-Maximilians-Univ. Munich
Hollenbach, D. J., & Salpeter, E. E. 1971, ApJ, 163, 155
Hollenbach, D. J., Takahashi, T., & Tielens, A. G. G. M. 1991, ApJ, 377, 192 (HTT91)
Hollenbach, D. J., Werner, M. W., & Salpeter, E. E. 1971, ApJ, 163, 165
Howe, J. E., Jaffe, D. T., Genzel, R., & Stacey, G. J. 1991, ApJ, 373, 158
Jaffe, D. T., Zhou, S., Howe, J. E., Herrmann, F., Madden, S. C., Poglitsch, A., van der Werf, P. P., & Stacey, G. J. 1994, ApJ, 436, 203
Jura, M. 1974, ApJ, 191, 375
Köster, B., Störzer, H., Stutzki, J., & Sternberg, A. 1994, A&A, 284, 545
Lada, E. A., & Blitz, L. 1988, ApJ, 326, L69
Launay, J. M., & Roueff, E. 1977, A&A, 56, 289
Le Bourlot, J., Pineau des Forêts, G., Roueff, E., & Flower, D. R. 1993, A&A, 267, 233
Lee, T. A. 1968, ApJ, 152, 913
Luhman, M. L., Jaffe, D. T., Keller, L. D., & Pak, S. 1994, ApJ, 436, L185
———. 1995, PASP, 107, 184
Luhman, M. L., Jaffe, D. T., Sternberg, A., Herrmann, F., & Poglitsch, A. 1996, ApJ, submitted
Maddalena, R. J., Morris, M., Moscowitz, J., & Thaddeus, P. 1986, ApJ, 303, 375
Madden, S. C., Geis, N., Genzel, R., Herrmann, F., Jackson, J. M., Poglitsch, A., Stacey, G. J., & Townes, C. H. 1993, ApJ, 407, 579
Maloney, P., & Black, J. H. 1988, ApJ, 325, 389
Martin, C., Hurwitz, M., & Bowyer, S. 1990, ApJ, 354, 220
Mathis, J. S., Mezger, P. M., & Panagia, N. 1983, A&A, 128, 212
Matsuhara, H., et al. 1989, ApJ, 339, L67
Mizutani, K., et al. 1994, ApJS, 91, 613
Mochizuki, K., et al. 1994, ApJ, 430, L37
Pak, S., Jaffe, D. T., & Keller, L. D. 1996, ApJ, 457, L43
Plume, R., Jaffe, D. T., Tatematsu, K., & Evans, N. J., II. 1996, in preparation
Reach, W. T., Koo, B.-C., & Heiles, C. 1994, ApJ, 429, 672
Rieke, G. H., & Lebofsky, M. J. 1985, ApJ, 288, 618
Roger, R. S., & Dewdney, P. E. 1992, ApJ, 385, 536
Schloerb, F. P., & Loren, R. B. 1982, in Ann. NY Acad. Sci., 395, Symposium on the Orion Nebula to Honor Henry Draper, ed. A. E. Glassgold, P. J. Huggins, & E. L. Schucking, 32
Schulz, A., Güsten, R., Zylka, R., & Serabyn, E. 1991, A&A, 246, 570
Sellgren, K. 1986, ApJ, 305, 399
Shibai, H., et al. 1991, ApJ, 374, 522
Shull, J. M. 1978, ApJ, 219, 877

Shull, J. M., & Beckwith, S. 1982, ARA&A, 20, 163
Stacey, G. J., Geis, N., Genzel, R., Lugten, J. B., Poglitsch, A., Sternberg, A., & Townes, C. H. 1991, ApJ, 373, 423
Stacey, G. J., Jaffe, D. T., Geis, N., Genzel, R., Harris, A. I., Poglitsch, A., Stutzki, J., & Townes, C. H. 1993, ApJ, 404, 219
Sternberg, A. 1988, ApJ, 332, 400
———. 1989, in Proc. 22d ESLAB Symp., Infrared Spectroscopy in Astronomy, ed. A. C. H. Glasse, M. F. Kessler, R. Gonzalez-Riestra, & B. H. Kaldeich (ESA SP-290) (Paris: ESA), 269
———. 1992, in IAU Symp. 150, Astrochemistry of Cosmic Phenomena, ed. P. D. Singh (Dordrecht: Kluwer), 329
Sternberg, A., & Dalgarno, A. 1989, ApJ, 338, 197
Stutzki, J., Stacey, G. J., Genzel, R., Harris, A. I., Jaffe, D. T., & Lugten, J. B. 1988, ApJ, 332, 379
Tanaka, M., Hasegawa, T., Hayashi, S. S., Brand, P. W. J. L., & Gatley, I. 1989, ApJ, 336, 207
Thompson, R. I., Thronson, H. A., Jr., & Campbell, B. G. 1981, ApJ, 249, 622
Thronson, H. A., Jr., Harper, D. A., Keene, J., Loewenstein, R. F., Moseley, H. S., & Telesco, C. M. 1978, AJ, 83, 492
Thronson, H. A., Jr., Lada, C. J., Schwartz, P. R., Smith, H. A., Smith, J., Glaccum, W., Harper, D. A., & Loewenstein, R. F. 1984, ApJ, 280, 154
Tielens, A. G. G. M., & Hollenbach, D. J. 1985a, ApJ, 291, 722
———. 1985b, ApJ, 291, 747
Turner, J., Kirby-Docken, K., & Dalgarno, A. 1977, ApJS, 35, 281
van Dishoeck, E. F., & Black, J. H. 1988, ApJ, 334, 771
Whittet, D. C. B. 1974, MNRAS, 168, 371
Wolfire, M. G., Hollenbach, D. J., & Tielens, A. G. G. M. 1989, ApJ, 344, 770
Wright, E. L., et al. 1991, ApJ, 381, 200